

## DETECTION OF THE ENERGETIC PULSAR PSR B1509–58 AND ITS PULSAR WIND NEBULA IN MSH 15–52 USING THE *FERMI*-LARGE AREA TELESCOPE

A. A. ABDO<sup>1,2</sup>, M. ACKERMANN<sup>3</sup>, M. AJELLO<sup>3</sup>, A. ALLAFORT<sup>3</sup>, K. ASANO<sup>4</sup>, L. BALDINI<sup>5</sup>, J. BALLE<sup>6</sup>, G. BARBIELLINI<sup>7,8</sup>, M. G. BARING<sup>9</sup>, D. BASTIERI<sup>10,11</sup>, K. BECHTOL<sup>3</sup>, R. BELLAZZINI<sup>5</sup>, B. BERENJI<sup>3</sup>, R. D. BLANDFORD<sup>3</sup>, E. D. BLOOM<sup>3</sup>, E. BONAMENTE<sup>12,13</sup>, A. W. BORGLAND<sup>3</sup>, J. BRIGEON<sup>5</sup>, A. BREZ<sup>5</sup>, M. BRIGIDA<sup>14,15</sup>, P. BRUEL<sup>16</sup>, S. BUSON<sup>10</sup>, G. A. CALIANDRO<sup>17</sup>, R. A. CAMERON<sup>3</sup>, F. CAMILO<sup>18</sup>, P. A. CARAVEO<sup>19</sup>, S. CARRIGAN<sup>11</sup>, J. M. CASANDJIAN<sup>6</sup>, C. CECCHI<sup>12,13</sup>, Ö. ÇELİK<sup>20,21,22</sup>, A. CHEKHTMAN<sup>1,23</sup>, C. C. CHEUNG<sup>1,2</sup>, J. CHIANG<sup>3</sup>, S. CIPRINI<sup>13</sup>, R. CLAUS<sup>3</sup>, J. COHEN-TANUGI<sup>24</sup>, J. CONRAD<sup>25,26,60</sup>, P. R. DEN HARTOG<sup>3</sup>, C. D. DERMER<sup>1</sup>, A. DE LUCA<sup>27</sup>, F. DE PALMA<sup>14,15</sup>, M. DORMODY<sup>28</sup>, E. DO COUTO E SILVA<sup>3</sup>, P. S. DRELL<sup>3</sup>, R. DUBOIS<sup>3</sup>, D. DUMORA<sup>29,30</sup>, C. FARNIER<sup>24</sup>, C. FAVUZZI<sup>14,15</sup>, S. J. FEGAN<sup>16</sup>, E. C. FERRARA<sup>20</sup>, W. B. FOCKE<sup>3</sup>, M. FRAILIS<sup>31,32</sup>, Y. FUKAZAWA<sup>33</sup>, S. FUNK<sup>3</sup>, P. FUSCO<sup>14,15</sup>, F. GARGANO<sup>15</sup>, N. GEHRELS<sup>20</sup>, S. GERMANI<sup>12,13</sup>, N. GIGLIETTO<sup>14,15</sup>, F. GIORDANO<sup>14,15</sup>, T. GLANZMAN<sup>3</sup>, G. GODFREY<sup>3</sup>, E. V. GOTTHELF<sup>18</sup>, I. A. GRENIER<sup>6</sup>, M.-H. GRONDIN<sup>29,30</sup>, J. E. GROVE<sup>1</sup>, L. GUILLEMOT<sup>29,30,34</sup>, S. GUIRIEC<sup>35</sup>, Y. HANABATA<sup>33</sup>, A. K. HARDING<sup>20</sup>, E. HAYS<sup>20</sup>, G. HOBBS<sup>36</sup>, D. HORAN<sup>16</sup>, R. E. HUGHES<sup>37</sup>, G. JÓHANNESSEN<sup>3</sup>, A. S. JOHNSON<sup>3</sup>, T. J. JOHNSON<sup>20,38</sup>, W. N. JOHNSON<sup>1</sup>, S. JOHNSTON<sup>36</sup>, T. KAMAE<sup>3</sup>, Y. KANAI<sup>39</sup>, G. KANBACH<sup>40</sup>, H. KATAGIRI<sup>33</sup>, J. KATAOKA<sup>41</sup>, N. KAWAI<sup>39,42</sup>, M. KEITH<sup>36</sup>, M. KERR<sup>43</sup>, J. KNÖDLSER<sup>44</sup>, M. KUSS<sup>5</sup>, J. LANDE<sup>3</sup>, L. LATRONICO<sup>5</sup>, M. LEMOINE-GOUMARD<sup>29,30</sup>, M. LLENA GARDE<sup>25,26</sup>, F. LONGO<sup>7,8</sup>, F. LOPARCO<sup>14,15</sup>, B. LOTT<sup>29,30</sup>, M. N. LOVELLETTE<sup>1</sup>, P. LUBRANO<sup>12,13</sup>, A. MAKEEV<sup>1,23</sup>, R. N. MANCHESTER<sup>36</sup>, M. MARELLI<sup>19</sup>, M. N. MAZZIOTTA<sup>15</sup>, J. E. MCENERY<sup>20,38</sup>, P. F. MICHELSON<sup>3</sup>, W. MITTHUMSIRI<sup>3</sup>, T. MIZUNO<sup>33</sup>, A. A. MOISEEV<sup>21,38</sup>, C. MONTE<sup>14,15</sup>, M. E. MONZANI<sup>3</sup>, A. MORSELLI<sup>45</sup>, I. V. MOSKALENKO<sup>3</sup>, S. MURCIA<sup>3</sup>, T. NAKAMORI<sup>39</sup>, P. L. NOLAN<sup>3</sup>, J. P. NORRIS<sup>46</sup>, E. NUSS<sup>24</sup>, M. OHNO<sup>47</sup>, T. OHSUGI<sup>48</sup>, N. OMODEI<sup>3</sup>, E. ORLANDO<sup>40</sup>, J. F. ORMES<sup>46</sup>, D. PANEQUE<sup>3</sup>, J. H. PANETTA<sup>3</sup>, D. PARENT<sup>1,23,29,30</sup>, V. PELASSA<sup>24</sup>, M. PEPE<sup>12,13</sup>, M. PESCE-ROLLINS<sup>5</sup>, F. PIRON<sup>24</sup>, T. A. PORTER<sup>3</sup>, S. RAINÒ<sup>14,15</sup>, R. RANDO<sup>10,11</sup>, M. RAZZANO<sup>5</sup>, N. REA<sup>17</sup>, A. REIMER<sup>3,49</sup>, O. REIMER<sup>3,49</sup>, T. REPOSEUR<sup>29,30</sup>, A. Y. RODRIGUEZ<sup>17</sup>, R. W. ROMANI<sup>3</sup>, M. ROTH<sup>43</sup>, F. RYDE<sup>26,50</sup>, H. F.-W. SADROZINSKI<sup>28</sup>, A. SANDER<sup>37</sup>, P. M. SAZ PARKINSON<sup>28</sup>, C. SGRÒ<sup>5</sup>, E. J. SISKIND<sup>51</sup>, D. A. SMITH<sup>29,30</sup>, P. D. SMITH<sup>37</sup>, G. SPANDRE<sup>5</sup>, P. SPINELLI<sup>14,15</sup>, J.-L. STARCK<sup>6</sup>, M. S. STRICKMAN<sup>1</sup>, D. J. SUSON<sup>52</sup>, H. TAKAHASHI<sup>48</sup>, T. TAKAHASHI<sup>47</sup>, T. TANAKA<sup>3</sup>, J. B. THAYER<sup>3</sup>, J. G. THAYER<sup>3</sup>, D. J. THOMPSON<sup>20</sup>, S. E. THORSETT<sup>28</sup>, L. TIBALDO<sup>6,10,11,61</sup>, D. F. TORRES<sup>17,53</sup>, G. TOSTI<sup>12,13</sup>, A. TRAMACERE<sup>3,54,55</sup>, Y. UCHIYAMA<sup>3</sup>, T. L. USHER<sup>3</sup>, V. VASILEIOU<sup>21,22</sup>, C. VENTER<sup>56</sup>, N. VILCHEZ<sup>44</sup>, V. VITALE<sup>45,57</sup>, A. P. WAITE<sup>3</sup>, P. WANG<sup>3</sup>, P. WELTEVREDE<sup>58</sup>, B. L. WINER<sup>37</sup>, K. S. WOOD<sup>1</sup>, Z. YANG<sup>25,26</sup>, T. YLINEN<sup>26,50,59</sup>, AND M. ZIEGLER<sup>28</sup>

<sup>1</sup> Space Science Division, Naval Research Laboratory, Washington, DC 20375, USA

<sup>2</sup> National Research Council Research Associate, National Academy of Sciences, Washington, DC 20001, USA

<sup>3</sup> W. W. Hansen Experimental Physics Laboratory, Kavli Institute for Particle Astrophysics and Cosmology, Department of Physics and SLAC National Accelerator Laboratory, Stanford University, Stanford, CA 94305, USA; [hartog@stanford.edu](mailto:hartog@stanford.edu)

<sup>4</sup> Interactive Research Center of Science, Tokyo Institute of Technology, Meguro City, Tokyo 152-8551, Japan

<sup>5</sup> Istituto Nazionale di Fisica Nucleare, Sezione di Pisa, I-56127 Pisa, Italy

<sup>6</sup> Laboratoire AIM, CEA-IRFU/CNRS/Université Paris Diderot, Service d'Astrophysique, CEA Saclay, 91191 Gif sur Yvette, France

<sup>7</sup> Istituto Nazionale di Fisica Nucleare, Sezione di Trieste, I-34127 Trieste, Italy

<sup>8</sup> Dipartimento di Fisica, Università di Trieste, I-34127 Trieste, Italy

<sup>9</sup> Department of Physics and Astronomy, Rice University, MS-108, P.O. Box 1892, Houston, TX 77251, USA

<sup>10</sup> Istituto Nazionale di Fisica Nucleare, Sezione di Padova, I-35131 Padova, Italy

<sup>11</sup> Dipartimento di Fisica "G. Galilei," Università di Padova, I-35131 Padova, Italy

<sup>12</sup> Istituto Nazionale di Fisica Nucleare, Sezione di Perugia, I-06123 Perugia, Italy

<sup>13</sup> Dipartimento di Fisica, Università degli Studi di Perugia, I-06123 Perugia, Italy

<sup>14</sup> Dipartimento di Fisica "M. Merlin" dell'Università e del Politecnico di Bari, I-70126 Bari, Italy

<sup>15</sup> Istituto Nazionale di Fisica Nucleare, Sezione di Bari, 70126 Bari, Italy

<sup>16</sup> Laboratoire Leprince-Ringuet, École polytechnique, CNRS/IN2P3, Palaiseau, France

<sup>17</sup> Institut de Ciències de l'Espai (IEEC-CSIC), Campus UAB, 08193 Barcelona, Spain

<sup>18</sup> Columbia Astrophysics Laboratory, Columbia University, New York, NY 10027, USA

<sup>19</sup> INAF-Istituto di Astrofisica Spaziale e Fisica Cosmica, I-20133 Milano, Italy

<sup>20</sup> NASA Goddard Space Flight Center, Greenbelt, MD 20771, USA

<sup>21</sup> Center for Research and Exploration in Space Science and Technology (CREST) and NASA Goddard Space Flight Center, Greenbelt, MD 20771, USA

<sup>22</sup> Department of Physics and Center for Space Sciences and Technology, University of Maryland Baltimore County, Baltimore, MD 21250, USA

<sup>23</sup> George Mason University, Fairfax, VA 22030, USA

<sup>24</sup> Laboratoire de Physique Théorique et Astroparticules, Université Montpellier 2, CNRS/IN2P3, Montpellier, France

<sup>25</sup> Department of Physics, Stockholm University, AlbaNova, SE-106 91 Stockholm, Sweden

<sup>26</sup> The Oskar Klein Centre for Cosmoparticle Physics, AlbaNova, SE-106 91 Stockholm, Sweden

<sup>27</sup> Istituto Universitario di Studi Superiori (IUSS), I-27100 Pavia, Italy

<sup>28</sup> Santa Cruz Institute for Particle Physics, Department of Physics and Department of Astronomy and Astrophysics, University of California at Santa Cruz, Santa Cruz, CA 95064, USA

<sup>29</sup> CNRS/IN2P3, Centre d'Études Nucléaires Bordeaux Gradignan, UMR 5797, Gradignan, 33175, France; [grondin@cenbg.in2p3.fr](mailto:grondin@cenbg.in2p3.fr), [lemoine@cenbg.in2p3.fr](mailto:lemoine@cenbg.in2p3.fr)

<sup>30</sup> Université de Bordeaux, Centre d'Études Nucléaires Bordeaux Gradignan, UMR 5797, Gradignan 33175, France

<sup>31</sup> Dipartimento di Fisica, Università di Udine and Istituto Nazionale di Fisica Nucleare, Sezione di Trieste, Gruppo Collegato di Udine, I-33100 Udine, Italy

<sup>32</sup> Osservatorio Astronomico di Trieste, Istituto Nazionale di Astrofisica, I-34143 Trieste, Italy

<sup>33</sup> Department of Physical Sciences, Hiroshima University, Higashi-Hiroshima, Hiroshima 739-8526, Japan

<sup>34</sup> Max-Planck-Institut für Radioastronomie, Auf dem Hügel 69, 53121 Bonn, Germany

<sup>35</sup> Center for Space Plasma and Aeronomic Research (CSPAR), University of Alabama in Huntsville, Huntsville, AL 35899, USA

<sup>36</sup> Australia Telescope National Facility, CSIRO, Epping, NSW 1710, Australia

<sup>37</sup> Department of Physics, Center for Cosmology and Astro-Particle Physics, The Ohio State University, Columbus, OH 43210, USA

- <sup>38</sup> Department of Physics and Department of Astronomy, University of Maryland, College Park, MD 20742, USA  
<sup>39</sup> Department of Physics, Tokyo Institute of Technology, Meguro City, Tokyo 152-8551, Japan; nakamori@hp.phys.titech.ac.jp  
<sup>40</sup> Max-Planck Institut für extraterrestrische Physik, 85748 Garching, Germany  
<sup>41</sup> Research Institute for Science and Engineering, Waseda University, 3-4-1 Okubo, Shinjuku, Tokyo 169-8555, Japan  
<sup>42</sup> Cosmic Radiation Laboratory, Institute of Physical and Chemical Research (RIKEN), Wako, Saitama 351-0198, Japan  
<sup>43</sup> Department of Physics, University of Washington, Seattle, WA 98195-1560, USA  
<sup>44</sup> Centre d'Étude Spatiale des Rayonnements, CNRS/UPS, BP 44346, F-30128 Toulouse Cedex 4, France  
<sup>45</sup> Istituto Nazionale di Fisica Nucleare, Sezione di Roma "Tor Vergata," I-00133 Roma, Italy  
<sup>46</sup> Department of Physics and Astronomy, University of Denver, Denver, CO 80208, USA  
<sup>47</sup> Institute of Space and Astronautical Science, JAXA, 3-1-1 Yoshinodai, Sagami-hara, Kanagawa 229-8510, Japan  
<sup>48</sup> Hiroshima Astrophysical Science Center, Hiroshima University, Higashi-Hiroshima, Hiroshima 739-8526, Japan  
<sup>49</sup> Institut für Astro- und Teilchenphysik and Institut für Theoretische Physik, Leopold-Franzens-Universität Innsbruck, A-6020 Innsbruck, Austria  
<sup>50</sup> Department of Physics, Royal Institute of Technology (KTH), AlbaNova, SE-106 91 Stockholm, Sweden  
<sup>51</sup> NYCB Real-Time Computing Inc., Lattingtown, NY 11560-1025, USA  
<sup>52</sup> Department of Chemistry and Physics, Purdue University Calumet, Hammond, IN 46323-2094, USA  
<sup>53</sup> Institució Catalana de Recerca i Estudis Avançats (ICREA), Barcelona, Spain  
<sup>54</sup> Consorzio Interuniversitario per la Fisica Spaziale (CIFS), I-10133 Torino, Italy  
<sup>55</sup> INTEGRAL Science Data Centre, CH-1290 Versoix, Switzerland  
<sup>56</sup> North-West University, Potchefstroom Campus, Potchefstroom 2520, South Africa  
<sup>57</sup> Dipartimento di Fisica, Università di Roma "Tor Vergata," I-00133 Roma, Italy  
<sup>58</sup> Jodrell Bank Centre for Astrophysics, School of Physics and Astronomy, The University of Manchester, M13 9PL, UK  
<sup>59</sup> School of Pure and Applied Natural Sciences, University of Kalmar, SE-391 82 Kalmar, Sweden  
Received 2010 January 20; accepted 2010 March 18; published 2010 April 15

## ABSTRACT

We report the detection of high-energy  $\gamma$ -ray emission from the young and energetic pulsar PSR B1509–58 and its pulsar wind nebula (PWN) in the composite supernova remnant G320.4–1.2 (aka MSH 15–52). Using 1 yr of survey data with the *Fermi*-Large Area Telescope (LAT), we detected pulsations from PSR B1509–58 up to 1 GeV and extended  $\gamma$ -ray emission above 1 GeV spatially coincident with the PWN. The pulsar light curve presents two peaks offset from the radio peak by phases  $0.96 \pm 0.01$  and  $0.33 \pm 0.02$ . New constraining upper limits on the pulsar emission are derived below 1 GeV and confirm a severe spectral break at a few tens of MeV. The nebular spectrum in the 1–100 GeV energy range is well described by a power law with a spectral index of  $(1.57 \pm 0.17 \pm 0.13)$  and a flux above 1 GeV of  $(2.91 \pm 0.79 \pm 1.35) \times 10^{-9} \text{ cm}^{-2} \text{ s}^{-1}$ . The first errors represent the statistical errors on the fit parameters, while the second ones are the systematic uncertainties. The LAT spectrum of the nebula connects nicely with Cherenkov observations, and indicates a spectral break between GeV and TeV energies.

**Key words:** ISM: individual objects (G320.4–1.2, MSH 15–52) – pulsars: individual (PSR B1509–58, PSR J1513–5908)

*Online-only material:* color figures

## 1. INTRODUCTION

Pulsars and pulsar wind nebulae (PWNe) are believed to be sources of cosmic-ray electrons (e.g., Kennel & Coroniti 1984; Gaensler & Slane 2006). Although hadronic  $\gamma$ -ray emission from TeV emitting PWNe has been suggested by many authors (e.g., Bednarek & Bartosik 2003; Horns 2006), most evidence indicates that  $\gamma$ -rays are generated via inverse Compton scattering of electrons accelerated in pulsar magnetospheres and at pulsar wind termination shocks.

The composite supernova remnant (SNR) G320.4–1.2 (aka MSH 15–52; Caswell et al. 1981) is usually associated with the rotation-powered radio pulsar PSR B1509–58 (aka PSR J1513–5908). The 150 ms rotation period was discovered by the *Einstein* satellite (Seward & Harden 1982) and soon thereafter confirmed in the radio domain (Manchester et al. 1982). With a large period derivative ( $1.5 \times 10^{-12} \text{ s s}^{-1}$ ), this pulsar is one of the youngest and most energetic pulsars known in the Galaxy with a characteristic age of 1700 yr and a spin-down power  $\dot{E}$  of  $1.8 \times 10^{37} \text{ erg s}^{-1}$ . The inferred surface magnetic field is  $1.5 \times 10^{13} \text{ G}$  derived under the assumption of

a dipolar magnetic field. The measurement of the pulsar braking index  $n = 2.839$  shows that this assumption is reasonable (e.g., Livingstone et al. 2005). Therefore, the high magnetic field is not much below the quantum-critical magnetic field of  $4.413 \times 10^{13} \text{ G}$ , the domain of the so-called high- $B$ -field pulsars and magnetars. The distance is estimated at  $5.2 \pm 1.4 \text{ kpc}$  using H I absorption measurements (Gaensler et al. 1999). This is consistent with the value of  $4.2 \pm 0.6 \text{ kpc}$  derived from the dispersion measure (Cordes & Lazio 2002). PSR B1509–58 has been studied by all major X-ray and  $\gamma$ -ray observatories yielding a broadband spectral energy distribution (SED) and pulse profiles as a function of energy. Its detection by COMPTEL (0.75–30 MeV; Kuiper et al. 1999) and non-detection with the Energetic Gamma-Ray Experiment Telescope (EGRET) in the 30 MeV–30 GeV energy range, both aboard the *Compton Gamma Ray Observatory* (CGRO), indicate an abrupt spectral break between 10 and 30 MeV. This break is well below the break energies of most  $\gamma$ -ray pulsars detected by *Fermi*, which are typically around a few GeV (Abdo et al. 2010a). More recently, the detection of pulsed  $\gamma$ -rays from PSR B1509–58 at  $4\sigma$  level above 100 MeV was reported by *AGILE* (Pellizzoni et al. 2009).

*Einstein* X-ray observations of MSH 15–52 revealed an elongated non-thermal source centered on the pulsar (Seward & Harden 1982), later confirmed by *ROSAT* and interpreted as a PWN powered by PSR B1509–58 (Trussoni et al. 1996). This

<sup>60</sup> Royal Swedish Academy of Sciences Research Fellow, funded by a grant from the K. A. Wallenberg Foundation.

<sup>61</sup> Partially supported by the International Doctorate on Astroparticle Physics (IDAPP) program.

PWN, composed of arcs and bipolar jets, is especially bright and extended in X-rays (Tamura et al. 1996; Gaensler et al. 2002; Forot et al. 2006; Yatsu et al. 2009), and at very high energies (Sako et al. 2000; Aharonian et al. 2005; Nakamori et al. 2008). The dimensions of the PWN as observed by *ROSAT* (Trussoni et al. 1996) and H.E.S.S. (Aharonian et al. 2005) are  $10' \times 6'$  and  $6.4' \times 2.3'$ , respectively. The multi-wavelength emission of the PWN in MSH 15–52 can be accounted for by synchrotron radiation from electrons within the PWN and inverse Compton scattering on soft photons such as the cosmic microwave background (CMB), the infrared (IR), and the optical interstellar radiation field (ISRF; Aharonian et al. 2005; Nakamori et al. 2008). This leptonic model requires a broken power-law spectrum for the electrons. However, large uncertainties on the break energy remain due to the lack of observations at corresponding wavelengths, namely, IR or optical for the synchrotron radiation and GeV  $\gamma$ -rays for the inverse Compton component. The observations performed now with *Fermi* help constrain the electron spectrum, in particular the break energy, of the PWN of MSH 15–52 and provide new elements to the discussion on the energetics.

Successfully launched in 2008 June, the Large Area Telescope (LAT) onboard the *Fermi* Gamma-ray Space Telescope covers the 20 MeV–300 GeV energy range. With its improved performance compared to its predecessor EGRET, it offers the opportunity to search for high-energy pulsations of PSR B1509–58, and, measuring the spectrum of the PWN in MSH 15–52, to better constrain the emission models in pulsar winds. The results of 1 yr observations of the pulsar PSR B1509–58 and its PWN are reported in the following sections.

## 2. RADIO TIMING OBSERVATIONS

With its large spin-down power, the pulsar PSR B1509–58 is a good candidate for  $\gamma$ -ray detection and is monitored by the LAT pulsar timing campaign (Smith et al. 2008) coordinated among *Fermi*, radio, and X-ray telescopes.

The ephemeris of the pulsar PSR B1509–58 used in the analysis of the *Fermi*-LAT data is obtained using observations at 1.4 GHz made with the 64 m Parkes radio telescope (Manchester 2008; Weltevrede et al. 2010). A total of 42 time of arrivals (TOAs) were recorded between 2007 April 30 and 2009 August 29. Radio observations simultaneous with the  $\gamma$ -ray data make it possible to correct for the large drift in phase caused by timing noise when constructing the  $\gamma$ -ray light curves.

The TEMPO2 timing package (Hobbs et al. 2006) is then used to build the timing solution from the 42 TOAs. We fit the TOAs to the pulsar rotation frequency and its first two derivatives. The fit further includes three harmonically related sinusoids, using the “FITWAVES” option in the TEMPO2 package, to flatten the timing noise. We used the value of  $DM = (252.5 \pm 0.3) \text{ cm}^{-3} \text{ pc}$  for the dispersion measure (Hobbs et al. 2004), given in the ATNF Pulsar Catalogue.<sup>62</sup> The post-fit rms is  $875 \mu\text{s}$ , or 0.6% of the pulsar phase. This timing solution is used in the temporal analysis described in detail in Section 4.1.1.

## 3. LAT DESCRIPTION AND DATA SELECTION

The LAT is a high-energy photon telescope sensitive to  $\gamma$ -rays with energies from below 20 MeV to more than 300 GeV that detects photons through pair conversion. The photon incident direction is derived by tracking the electron–positron pair in a high-resolution converter tracker and the energy is measured

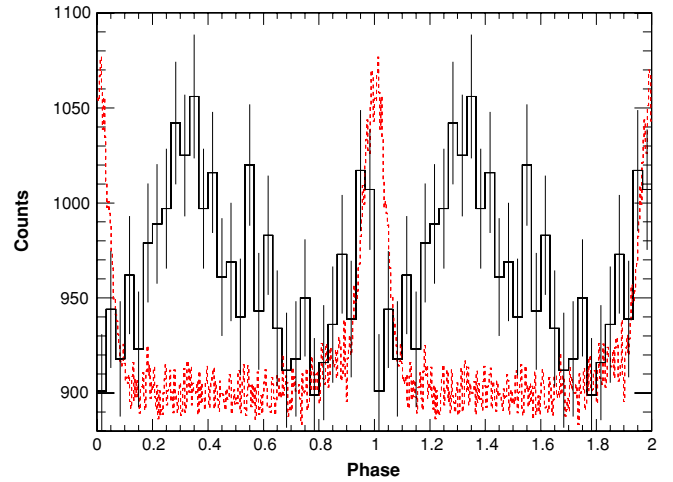


**Figure 1.** Light curve of the pulsar PSR B1509–58 above 30 MeV within an energy-dependent circular region, as described in Section 4.1.1. The light curve profile is binned to 1/30 of pulsar phase. The radio profile (red dashed line) is overlaid in arbitrary units. The main peak of the radio pulse seen at 1.4 GHz is at phase 0. Two cycles are shown.

(A color version of this figure is available in the online journal.)

with a CsI(Tl) crystal calorimeter. An anticoincidence detector identifies the background of charged particles (Atwood et al. 2009). In comparison to its predecessor EGRET, the LAT has a larger effective area ( $\sim 8000 \text{ cm}^2$  on-axis), a broader field of view ( $\sim 2.4 \text{ sr}$ ), and a superior angular resolution ( $\sim 0.6^\circ$ , 68% containment at 1 GeV for events converting in the front section of the tracker).

The analyses reported here are performed on 374 days of data taken in survey mode (2008 August 4 to 2009 August 13). Events from the “Diffuse” class are selected, i.e., the highest quality photon data, having the most stringent background rejection (Atwood et al. 2009). In addition, we exclude events with zenith angles greater than  $105^\circ$  to avoid contamination by  $\gamma$ -rays produced by cosmic-ray interactions in the Earth’s atmosphere and periods corresponding to a rocking angle (i.e., the angle between the viewing direction of the LAT and the zenith) larger than  $43^\circ$ .

## 4. RESULTS

### 4.1. Gamma-ray Emission from PSR B1509–58

#### 4.1.1. Light Curves

We selected photons with an angle  $\theta < \max(5.12 \times (\frac{E}{100 \text{ MeV}})^{-0.8}, 0.2)$ , where  $E$  is the energy of the photon, from the radio pulsar position, R.A. =  $(228.48175 \pm 0.00038)^\circ$ , decl. =  $(-59.13583 \pm 0.00028)^\circ$  in J2000 (Kaspi et al. 1994). The energy dependence of the integration radius is a satisfactory approximation of the shape of the LAT point-spread function (PSF), especially at low energies.

Photons in this energy-dependent region are then phase-folded using the timing solution described in Section 2. The resulting  $\gamma$ -ray light curve for energies higher than 30 MeV is presented in Figure 1. We have a total of 28,966  $\gamma$ -rays in the circular region of energy-dependent radius, among which are  $1267 \pm 515$  pulsed photons after background subtraction. The radio profile (red dashed line) obtained from the 42 radio observations included in the timing solution used for our analysis is overlaid in Figure 1 for comparison. In this analysis, phase 0 is defined as the maximum of the main radio peak observed at 1.4 GHz.

<sup>62</sup> <http://www.atnf.csiro.au/research/pulsar/psrcat/>

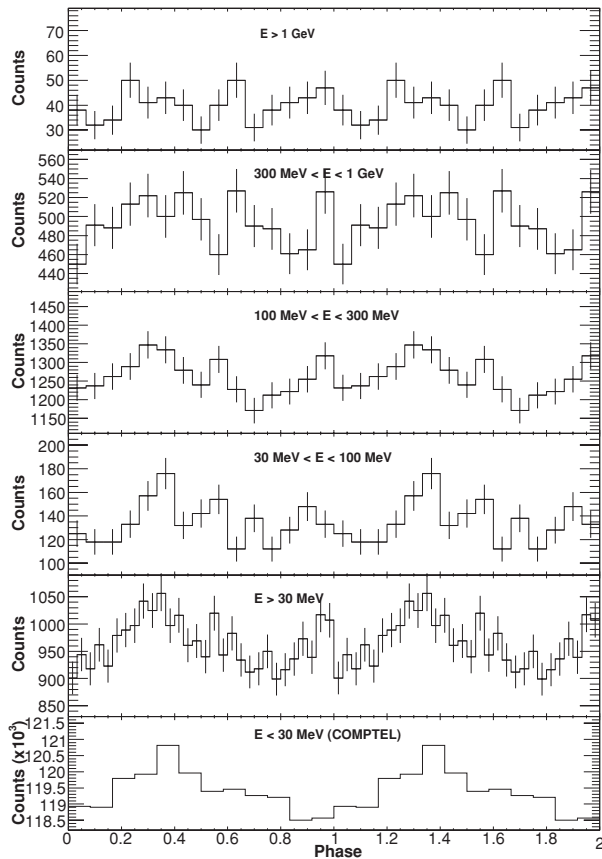


**Figure 2.** Light curves of the pulsar PSR B1509–58 in different energy bands within a circular region of energy-dependent radius. From bottom to top: COMPTEL (0.75–30 MeV; Kuiper et al. 1999) and LAT profiles in 30 MeV–300 GeV, 30–100 MeV, 100–300 MeV, 300 MeV–1 GeV, and 1–300 GeV energy bands are presented. Two cycles are shown.

In Figure 1, two peaks P1 and P2 can be observed at phases  $0.96 \pm 0.01$  and  $0.33 \pm 0.02$ , respectively. The uncertainty in the extrapolation of the radio pulse arrival time to infinite frequency, as defined in Manchester & Taylor (1977), is 0.004 in phase and can be neglected. Hence, the peaks are separated by  $\Delta\phi = 0.37 \pm 0.02$ . P1 and P2 are symmetric and can be well modeled by Lorentzian functions of half-widths of  $0.22 \pm 0.11$  and  $0.05 \pm 0.03$ , respectively. We also notice that the first  $\gamma$ -ray peak leads the radio main pulse by phase  $0.04 \pm 0.01$ , as shown in Figure 1, which corresponds to a delay of  $(6 \pm 2)$  ms.

Table 1 presents the value of the  $H$ -test as defined in de Jager et al. (1989) and obtained in the 30 MeV–100 GeV, 30–100 MeV, 100–300 MeV, 300 MeV–1 GeV, and 1–100 GeV energy bands using the energy-dependent circular radius defined above. The corresponding light curves are presented in Figure 2 along with the light curve measured by COMPTEL in the 0.75–30 MeV energy range (Kuiper et al. 1999). Within the error bars, the peak positions remain stable with energy. From Figure 2 and Table 1, we notice that no significant pulsation can be detected above 1 GeV. Using 374 days of data in survey mode, an  $H$ -test value of 31.34 is obtained in the 30 MeV–100 GeV energy range, corresponding to a significance of  $4.51\sigma$ .

#### 4.1.2. Spectral Analysis of PSR B1509–58

A spectral analysis of the pulsar is performed in the 100 MeV–1 GeV energy range using a maximum likelihood method (Mattox et al. 1996) implemented in the *Fermi* SSC

**Table 1**  
Results of the Periodicity Test Applied to PSR B1509–58 using the Energy-dependent Region Defined in Section 4.1.1

Energy Band (GeV)	$H$ -test	Significance ( $\sigma$ )
0.03–100	31.34	4.51
0.03–0.1	15.42	3.07
0.1–0.3	15.60	3.09
0.3–1.0	4.66	1.42
1.0–100	0.06	0.03

science tools as the *gtlike* code. This tool fits a source model to the data along with models for the instrumental, extragalactic, and Galactic backgrounds. In the following spectral analysis, the Galactic diffuse emission is modeled using the ring-hybrid model *gll\_iem\_v02.fit*. The instrumental background and the extragalactic radiation are described by a single isotropic component with a spectral shape described by the tabulated model *isotropic\_iem\_v02.txt*. These models and their detailed description are released by the LAT Collaboration.<sup>63</sup> Sources near the pulsar PSR B1509–58 found above the background with a statistical significance larger than  $5\sigma$  are extracted from the source list given in Abdo et al. (2010b), and are taken into account in this study. We use P6\_V3 post-launch instrument response functions (IRFs) that take into account pile-up and accidental coincidence effects in the detector subsystems.<sup>64</sup>

Despite the detection of pulsations, no significant  $\gamma$ -ray emission can be observed at the position of the pulsar using 374 days of LAT data. Indeed, most of the weak signal detected on PSR B1509–58 is observed at low energy (below 300 MeV) where the LAT angular resolution is large in comparison to the distance that separates our source of interest from the bright pulsar PSR J1509–5850 (less than  $0^\circ.8$ ). This renders the spectral analysis extremely complex. Therefore, only  $2\sigma$  upper limits can be derived and are presented in Figure 3. As an attempt to evaluate the flux of PSR B1509–58, pulsed excess counts were derived from the light curves (presented in Figure 2) in the 100–300 MeV and 300 MeV–1 GeV energy bands, as well as the corresponding effective area. The rapid increase of the effective area in the 100–300 MeV energy range (Atwood et al. 2009) makes the analysis highly dependent of the assumed spectral shape and yields very large errors on the flux estimate. Therefore, only the result obtained in the 300 MeV–1 GeV energy range (Atwood et al. 2009), where the effective area is more stable, is represented in Figure 3. The upper limit derived with *gtlike* in this energy band is consistent with the integrated flux estimated from the number of pulsed photons. The overall spectrum in the 1 keV–1 GeV energy range indicates a very low cutoff or break energy in the pulsar spectrum, as suggested by Kuiper et al. (1999). The implications of such upper limits on the emission models in pulsar magnetospheres are further discussed in Section 5.1.

## 4.2. High-energy Analysis of the PWN in MSH 15–52

### 4.2.1. Morphology

Figure 4 presents the smoothed counts maps of the region around MSH 15–52 in Galactic coordinates above 1 GeV (top panel) and 10 GeV (bottom panel) and binned in square pixels of

<sup>63</sup> *Fermi* Science Support Center: <http://fermi.gsfc.nasa.gov/ssc/>

<sup>64</sup> See [http://fermi.gsfc.nasa.gov/ssc/data/analysis/documentation/Cicerone/Cicerone\\_LAT\\_IRFs/IRF\\_overview.html](http://fermi.gsfc.nasa.gov/ssc/data/analysis/documentation/Cicerone/Cicerone_LAT_IRFs/IRF_overview.html) for more details.

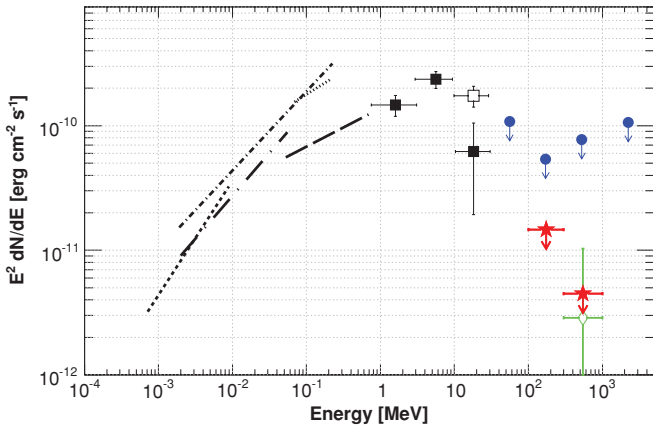


**Figure 3.** Spectrum of PSR B1509–58 from soft X-rays to  $\gamma$ -rays.  $2\sigma$  upper limits derived with *glike* from LAT observations are represented by red stars. The green diamond represents the integrated flux derived from the light curves and estimates of the effective area and exposure in the 300 MeV–1 GeV energy range, as described in Section 4.1.2. The filled squares are the COMPTEL flux points derived from the excess counts in the 0.15–0.65 phase range, while the open square represents the 10–30 MeV flux in the 0.15–0.65 phase interval above the spatially determined background. The blue circles are the  $2\sigma$  upper limits for the total fluxes obtained by EGRET. The different lines represent the best spectral fit measured by *ASCA* (short-dashed line, 0.7–10 keV), *Ginga* (dot-long-dashed line, 2–60 keV), *CGRO-OSSE* (long-dashed line, 50–750 keV), *WELCOME* (dotted line, 94–240 keV), and *RXTE* (dot-short-dashed line, 2–250 keV); see Kuiper et al. (1999) and references therein.

(A color version of this figure is available in the online journal.)

side length  $0^{\circ}05$ . The H.E.S.S. (Aharonian et al. 2005) contours have been overlaid in black for comparison. At low energies, the emission is essentially dominated by the bright nearby pulsar PSR J1509–5850 (Abdo et al. 2010a), marked by a blue star, whereas the significant  $\gamma$ -ray emission above 10 GeV is spatially coincident with the nebula in MSH 15–52. The position of the pulsar PSR B1509–58 is also marked with a blue star.

An analysis tool, *Sourcelike*, developed by the LAT Collaboration allows us to estimate the position and the size of the source, assuming a spatial and spectral model for the diffuse emission and different morphologies: a point source, a Gaussian shape, and a uniform disk. In this method, the likelihood is iterated to the data set assuming spatial source models, taking into account nearby sources, Galactic diffuse, and isotropic components in the fits (Abdo et al. 2010c), as described in Section 4.1.2.

Morphological studies are performed above 6.4 GeV, assuming the three spatial hypotheses mentioned above. The choice of this energy is motivated by the better angular resolution, the non-contamination from the Galactic diffuse emission, and nearby bright sources such as the pulsar PSR J1509–5850. The positions, extensions, and the corresponding errors as well as the Test Statistics (TS) obtained for each hypothesis are summarized in Table 2. The TS values are obtained as  $TS = 2(L_1 - L_0)$ , where  $L_0$  and  $L_1$  are the values of the log-likelihood obtained by null hypothesis and each source hypothesis, respectively. In view of the errors of localization, the fit positions are compatible with each other, and best fits are obtained either with a uniform disk (TS of 69.4) or a Gaussian distribution (TS of 67.6).

The differences in TS between the two extended shapes and the point-source hypotheses:  $TS_{\text{ext}} = 24.7$  and 22.9 for the uniform disk of extension  $\sigma \sim 0^{\circ}25$  and the Gaussian shape of extension  $\sigma \sim 0^{\circ}15$ , respectively, with relation to a point source, indicate a significant extension for the LAT source spatially coincident with the PWN in MSH 15–52. The conversion of the extensions obtained for the uniform disk and Gaussian

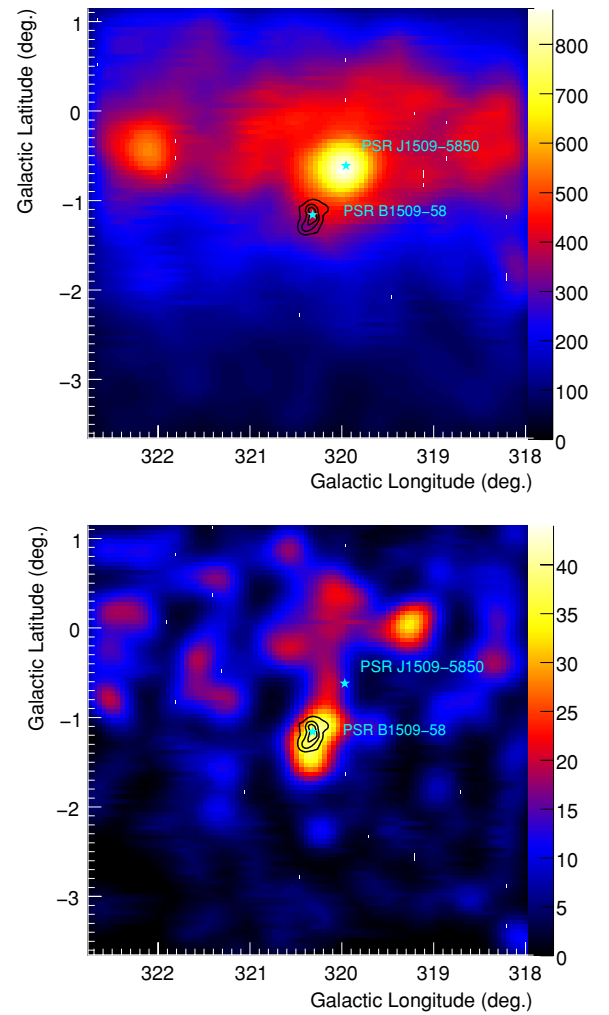


**Figure 4.** Smoothed counts maps in arbitrary units of the region around MSH 15–52 above 1 GeV (top) and 10 GeV (bottom) in Galactic coordinates, binned in square pixels of side length  $0^{\circ}05$ . The maps are smoothed with a Gaussian of  $\sigma = 0^{\circ}15$ . The H.E.S.S. (Aharonian et al. 2005) contours of the PWN in MSH 15–52 are overlaid in black for comparison. The positions of the pulsars PSR J1509–5850 and PSR B1509–58 are marked by blue stars.

(A color version of this figure is available in the online journal.)

**Table 2**  
Position of the Centroid, Extension, and Significance of the PWN in MSH 15–52 Obtained with *Sourcelike* Applied to the LAT Data

Spatial Model	Galactic Longitude (deg)	Galactic Latitude (deg)	Error (deg)	Radius (deg)	Test Statistics
Point source	320.288	–1.209	0.028		44.7
Gaussian	320.275	–1.266	0.051	$0.146 \pm 0.023$	67.6
Uniform disk	320.270	–1.271	0.061	$0.249 \pm 0.047$	69.4

distribution into an rms value gives results consistent with each other. In the following analyses, the spectral results obtained for the extended scenarios are presented. For comparison, the results derived assuming a point-source hypothesis are also quoted.

#### 4.2.2. Spectral Analysis

The following spectral analyses are performed using *glike*. *Sourcelike*, described in Section 4.2.1, is also run as a crosscheck and gives compatible results. The models used to describe the Galactic, extragalactic, and instrumental components are mentioned in Section 4.1.2. Sources near the PWN with a

**Table 3**  
Spectral Parameters of the PWN Obtained with *gtlike* for Different Spatial Models

Spatial Model	Flux Above 1 GeV ( $10^{-9} \text{ cm}^{-2} \text{ s}^{-1}$ )	Spectral Index
Point source	$2.00 \pm 0.76$	$1.57 \pm 0.24$
Gaussian	$3.01 \pm 0.81$	$1.58 \pm 0.17$
Uniform disk	$2.91 \pm 0.79$	$1.57 \pm 0.17$
H.E.S.S.	$2.22 \pm 0.77$	$1.52 \pm 0.21$

**Note.** Statistical errors only are quoted.

statistical significance larger than  $5\sigma$  are extracted from Abdo et al. (2010b), and are taken into account in this study.

Since the pulsar PSR B1509–58 is seen only below 1 GeV, the  $\gamma$ -ray photons in the 1–300 GeV energy range, in a  $20^\circ \times 20^\circ$  square centered on the pulsar radio position and coming from the entire pulse phase interval are selected.

The spectral analysis is performed above 1 GeV assuming different morphologies for the source: a point source, a Gaussian shape, and a uniform disk using the positions and extensions summarized in Table 2. A spectral fit using the H.E.S.S. image of the PWN (Aharonian et al. 2005) as a template is also performed. In this energy range, for all spatial distributions, the LAT spectrum can be well modeled by a simple power law

$$\frac{dN}{dE} \propto \left( \frac{E}{1 \text{ GeV}} \right)^{-\Gamma} \text{ cm}^{-2} \text{ s}^{-1} \text{ MeV}^{-1}, \quad (1)$$

where  $\Gamma$  is the photon index of the spectrum. The integrated fluxes and spectral indices of the source obtained for different spatial hypotheses are summarized in Table 3. The best fit is obtained for a uniform disk hypothesis, favored with respect to the Gaussian, H.E.S.S. template, and point-source morphologies with differences in TS of 3.9, 13.7, and 32.9, respectively. The LAT spectrum for a disk hypothesis is well described by a power law with a spectral index of  $(1.57 \pm 0.17 \pm 0.13)$  and a flux above 1 GeV of  $(2.91 \pm 0.79 \pm 1.35) \times 10^{-9} \text{ cm}^{-2} \text{ s}^{-1}$ . The first errors represent the statistical error on the fit parameters, while the second ones are the systematic uncertainties.

Three different uncertainties can affect the LAT spectrum estimation, as described in Abdo et al. (2010d). The first one is due to the uncertainty in the Galactic diffuse emission since MSH 15–52 is located close to the Galactic plane. Different versions of the Galactic diffuse emission generated by GALPROP (Strong et al. 2004a, 2004b) were used to estimate this error. The difference with the best diffuse model is found to be less than 6%. This implies systematic errors on the fluxes of 33% above 1 GeV. The second systematic is related to the morphology of the LAT source. As described in Table 2, the Gaussian, disk hypotheses, and the H.E.S.S. template match the gamma-ray morphology quite well. The fact that we cannot decide which one is better adapted induces an additional systematical error on the flux of the order of 24% above 1 GeV. The third systematic is produced by the uncertainties in the LAT IRFs. We bracket the energy-dependent effective area with envelopes above and below the nominal curves by linearly connecting differences of (10%, 5%, 20%) at  $\log(E/1 \text{ MeV})$  of (2, 2.75, 4), respectively, which yields additional errors on the flux and spectral index.

The SED of the PWN in the case of a uniform disk hypothesis is presented in Figure 5. The *Fermi*-LAT spectral points were obtained by dividing the 1–100 GeV range into six logarithmically spaced energy bins and performing a maximum likelihood

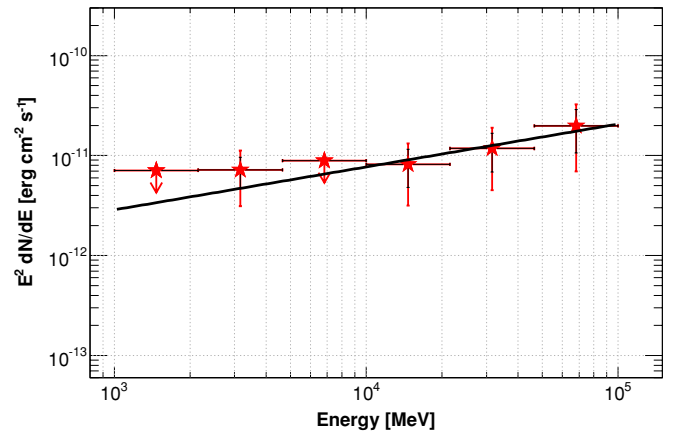


**Figure 5.** SED of the PWN above 1 GeV. The black line represents the results of the fit on the 1–100 GeV energy band. The spectral points are obtained using the model-independent maximum likelihood method described in Section 4.2.2.  $2\sigma$  upper limits are computed when the statistical significance of the energy interval is lower than  $3\sigma$ . The statistical errors are shown in black, while the red lines take into account both the statistical and systematic errors. Horizontal bars delimit the energy intervals.

(A color version of this figure is available in the online journal.)

spectral analysis in each interval, assuming a power-law shape for the source. These points provide a model-independent maximum likelihood spectrum, and are overlaid with the fitted model over the total energy range (black line).  $2\sigma$  upper limits are derived in energy bands where the significance level of the signal is lower than  $3\sigma$ .

## 5. DISCUSSION

### 5.1. High-energy Emission from PSR B1509–58

The improved performance of the *Fermi*-LAT compared to its predecessor EGRET allows the first detection of pulsations from PSR B1509–58 up to 1 GeV with a light curve presenting two peaks at phases  $0.96 \pm 0.01$  and  $0.33 \pm 0.02$  as seen in Figure 1. The alignment of the broad peak (P2) at phase  $\phi = 0.33$  is in general agreement with measurements of the phase of the main pulse by other high-energy experiments, e.g.,  $0.38 \pm 0.03$  with COMPTEL (10–30 MeV; Kuiper et al. 1999),  $0.32 \pm 0.02$  with *CGRO*-BATSE and *CGRO*-OSSE (20–500 keV; Ulmer et al. 1993), and  $\sim 0.35$  with *AGILE* (0.1–30 GeV; Pellizzoni et al. 2009). In X-rays, the peak shifts toward phase 0.24–0.27 (e.g., Kawai et al. 1991; Rots et al. 1998; Cusumano et al. 2001). We do not detect the suggested narrow pulsed component located at phase  $\sim 0.85$  reported by Kuiper et al. (1999) using combined COMPTEL and EGRET data in the 10–100 MeV energy range. However, we observe a pulse component at phase  $0.96 \pm 0.01$ . Considering the marginal significance of the COMPTEL/EGRET pulse, these peaks might be one single component. *AGILE* also observed a possible peak at phase  $\sim 0.85$  (Pellizzoni et al. 2009), which appears to be broader than the COMPTEL pulse. The detection of the narrow pulse only above 10 MeV strongly suggests a harder spectrum for this component than for the broad one.

The *Fermi* pulse shapes can be modeled with symmetric Lorentzian functions with half-widths of  $0.08 \pm 0.06$  and  $0.21 \pm 0.09$  for P1 and P2, respectively. Below MeV energies, the broad component is asymmetric. Its profile can be described with two Gaussian components (e.g., Kuiper et al. 1999; Cusumano et al. 2001). These components peak at phases  $\sim 0.25$  and  $\sim 0.39$  with widths of 0.056 and 0.129, respectively. Above a few tens

of MeV, it seems that the first of the two components is no longer contributing to the pulse profile, causing the apparent “shift,” as observed by Kuiper et al. (1999): the COMPTEL broad peak can be described with one single component. Within errors, the widths of the broad peak measured by COMPTEL and *Fermi* are in agreement.

The pulse component observed at phase  $0.96 \pm 0.01$  leads the 1.4 GHz radio pulse by  $0.04 \pm 0.01$  in phase. This feature is quite remarkable as so far all radio-loud pulsars excluding millisecond pulsars detected by *Fermi* present phase lags with respect to the radio pulse (Abdo et al. 2010a). However, the first  $\gamma$ -ray peak of the Crab pulsar precedes the main radio peak, but the high-energy peak lags the radio precursor (e.g., Abdo et al. 2010e). In the case of PSR B1509–58, a weak component was reported by Crawford et al. (2001) at 1351 MHz, which precedes the main pulse by  $\sim 0.14$  in phase. This might be a precursor as is seen in the Crab, but this has to be confirmed before we draw conclusions based on this possible feature.

Before *Fermi* launched, one of the major open questions dealt with the zone of gamma-ray production in pulsar magnetospheres. There are two classes of models that differ by the location of the emission region. First, polar-cap (PC) models place the emission near the magnetic poles of the neutron star (Daugherty & Harding 1996). The second class is formed by the outer-gap (OG) models (e.g., Cheng et al. 1986; Romani 1996), where the emission extends between the null charge surface and the light cylinder, and by the two-pole caustic (TPC) models (e.g., Dyks & Rudak 2003) which might be realized in slot gap (SG) acceleration models (e.g., Muslimov & Harding 2004), where the emission takes place between the neutron star surface and the light cylinder along the last open field line. After one year of *Fermi* observations, the high-altitude models seem to be favored, even if these models do not work for all pulsars. From previous high-energy observations, it was not obvious beforehand whether the high-energy emission from PSR B1509–58 could be described by surface or OG emission.

The  $\gamma$ -ray pulse profiles can be used to constrain the geometry of the pulsar. Watters et al. (2009) simulated a population of young spin-down-powered pulsars for vacuum-dipole magnetospheres. The peak separation of the  $\gamma$ -ray pulse profile presented in Figure 1 and the radio lag can yield constraints on the viewing angle  $\zeta$  and the magnetic inclination  $\alpha$ .

Using the heuristic law for the  $\gamma$ -ray luminosity (Watters et al. 2009)

$$L_\gamma \approx \eta \dot{E} \approx C \times \left( \frac{\dot{E}}{10^{33} \text{ erg s}^{-1}} \right)^{1/2} \times 10^{33} \text{ erg s}^{-1}, \quad (2)$$

with  $C$  a slowly varying function of the order of unity, the  $\gamma$ -ray efficiency  $\eta$  is estimated at 0.007. Assuming a  $\gamma$ -ray peak separation of  $0.37 \pm 0.02$  and a  $\gamma$ -ray efficiency of  $\eta = 0.01$ , the closest value to the real  $\gamma$ -ray efficiency that can be found in Watters et al. (2009) yields a tight constraint for  $\zeta$  in the range  $64^\circ$ – $70^\circ$  and  $\alpha$  values of  $45^\circ$ – $65^\circ$  in the framework of the OG model. The pulse profile can also be explained with the TPC model assuming  $\zeta$  of  $50^\circ$ – $65^\circ$  and  $\alpha$  of  $45^\circ$ – $65^\circ$ . However, the radio delay with respect to the first  $\gamma$ -ray peak could not be explained neither by the TPC nor the OG models.

Constraints on  $\alpha$  and  $\zeta$  are also possible with radio-polarization measurements (e.g., Radhakrishnan & Cooke 1969; Lyne & Manchester 1988). Polarization measurements by Crawford et al. (2001) show highly linearly polarized signals of 97% and 94% at 660 MHz and 1351 MHz, respectively.

However, the position angle shows only a shallow swing, which suggests a large magnetic-pole impact angle  $\beta = \zeta - \alpha$ . Magnetic inclination angles larger than  $60^\circ$  are excluded, in agreement with the maximum values of  $\beta$  derived using the OG and TPC models of  $25^\circ$  and  $20^\circ$ , respectively.

From the spectral analysis, the stringent upper limits of the pulsed spectrum measured by *Fermi*-LAT and presented in Figure 3 confirm the spectral break between 10 and 30 MeV suggested by Kuiper et al. (1999). However, the new  $2\sigma$  upper limits obtained with *Fermi* give more stringent constraints than EGRET’s one. The emission models can now be tested against these constraints.

Romani (1996) modeled the high-energy emission based on curvature radiation-reaction-limited charges in the outer magnetosphere and argued that, for high-field pulsars such as PSR B1509–58, synchrotron flux will dominate the emission in the 100 keV–10 MeV band, and more specifically the GeV band curvature component. The reason for this is that high-altitude two-photon pair creation in collisions between X-rays and hard gamma-rays is prolific, enhanced by aberration effects. This process will curtail super-GeV flux while permitting synchrotron emission at lower energies by electrons with  $\sim 0.3$ – $10$  GeV energies. In this way, the radiative power is transferred in cascading from the super-GeV band to a  $\lesssim 10$  MeV synchrotron window, i.e., generating a spectrum peaking below the *Fermi*-LAT energy range. Based on the three-dimensional outer-magnetosphere model of pulsars proposed by Cheng et al. (2000), Zhang & Cheng (2001) calculated the light curves and spectra of PSR B1509–58 assuming  $\alpha = 65^\circ$  and  $\zeta = 75^\circ$ . Their light curve presents a single broad peak comparable with the RXTE pulse profile, though a bit too narrow (Rots et al. 1998). The resulting spectrum is characterized by a simple power law from the soft X-ray band to a few hundred keV, with a photon index of 1.5 and a cutoff below 1 MeV. This overall shape agrees well with the multi-wavelength data available even though the proposed cutoff lies at an energy slightly smaller than that proposed by Kuiper et al. (1999) which is consistent with the new LAT data. Furthermore, their light curve presents a single broad peak, while a second peak is observed with the LAT data above 30 MeV.

Harding et al. (1997) argued that the PC model could explain the low spectral cutoff observed by *CGRO* for PSR B1509–58. Curvature emission at low altitudes would naturally appear at energies above 10 GeV, which was obviously not seen by EGRET and cannot be discerned in the LAT data presented here. Spectral attenuation by magnetic pair creation  $\gamma B \rightarrow e^+e^-$  would be extremely effective at energies above 100 MeV in the scenario of Harding et al. (1997). Using Equation (1) of Baring (2004), the maximum photon energy consistent with magnetic pair production transparency at altitude  $r$  along the last open field line is  $E_{\text{max}} \sim 1.76(B_{12})^{-1} P^{1/2} (r/R_*)^{7/2}$  GeV, for a surface polar field strength of  $B_0 = 10^{12} B_{12}$  G and stellar radius  $R_* \sim 10^6$  cm.  $B_0 \sim 1.5 \times 10^{13}$  G and  $P = 0.15$  s, then set  $E_{\text{max}} \sim 45(r/R_*)^{7/2}$  MeV for the energy of the  $\gamma B$  pair creation turnover. Even at the stellar surface, this estimate is too high to accommodate the EGRET upper limits and COMPTEL data downturn at around 10 MeV as seen in Figure 3.

However, as emphasized by Harding et al. (1997), magnetic photon splitting, a quantum-electrodynamic process important only for magnetic fields approaching the quantum critical value  $B_{\text{cr}} = 4.413 \times 10^{13}$  G, can attenuate  $\gamma$ -rays emitted near the surface of strongly magnetized pulsars. Harding et al. (1997) showed that photon splitting will be important for  $\gamma$ -ray pulsars

having a surface magnetic field larger than  $0.3B_{cr}$ , where the splitting attenuation lengths and escape energies become comparable to or less than those for pair production. Specifically, they demonstrated that attenuation due to photon splitting would reduce  $E_{max}$  to nicely accommodate the *CGRO* observations, but only if the emission was predominant at  $r \sim R_*$  and its co-latitude was consistent with a standard PC in PSR B1509–58. The new *Fermi*-LAT data with the combined soft X-ray to soft  $\gamma$ -ray (COMPTEL) spectral points confirm this picture: the PC model is spectroscopically viable for this pulsar, but subject to the strong constraint of emission at the magnetic co-latitude of the rim, i.e.,  $\sim 2^\circ$  as proposed by Kuiper et al. (1999). Higher altitudes and accompanying larger co-latitudes will push  $E_{max}$  to energies above 50 MeV. Accordingly, the LAT suggestion of modest pulsations up to energies almost as high as 1 GeV indicates that some portion of this emission might emanate from altitudes well above the stellar surface, where photon splitting will play a minimal role.

Although there are only upper limits on the pulsed spectrum in the LAT energy range at this point, the emission from both components of the light curve seems to extend to 1 GeV. The broad peak at phase 0.33 is consistent with outer magnetosphere geometry and is also roughly in phase with the COMPTEL peak. If it is assumed that the radio peak arises at small magnetic co-latitudes, then the radio/soft  $\gamma$ -ray phase separation suggests that both the *Fermi* and COMPTEL emission components at this phase originate in the outer magnetosphere, but given the sharp cutoff just above COMPTEL energies they must have different mechanisms. The narrow *Fermi* peak at phase 0.96 just leading the radio peak has no counterpart at COMPTEL energies but given its extension to 1 GeV and the magnetic pair and photon splitting attenuation limits discussed above, this peak must also originate in the outer magnetosphere. However, its phase location is not easily explained by current outer magnetosphere gap models. High-altitude pair-starved PC emission has been shown to produce a single peak just leading the radio pulse (Venter et al. 2009) and could potentially explain this component of the light curve at a similar  $\alpha$  and  $\zeta$  range. However, explaining both *Fermi* light curve peaks would require both pair-starved and non-pair-starved (gap) models to co-exist.

One might expect the high magnetic field of PSR B1509–58 to be the main reason for its unique behavior. This seems not to be the case if one compares PSR B1509–58 with the other pulsar *Fermi* has detected with an inferred surface magnetic field above  $10^{13}$  G: the nearby (1.4 kpc) PSR J0007+7303 (Abdo et al. 2008, 2010a) has a period of 314 ms and a period derivative of  $3.61 \times 10^{13} \text{ s}^{-1}$ . Its inferred surface magnetic field is  $1.1 \times 10^{13}$  G. The two pulsars behave very differently in spite of their similar magnetic fields. Indeed, PSR J0007+7303 belongs to the top 10 brightest  $\gamma$ -ray pulsars and has a hard power-law spectrum with photon index  $\Gamma = 1.38$  with a spectral cutoff energy at 4.6 GeV. Its spin-down power ( $4.5 \times 10^{35} \text{ erg s}^{-1}$ ) is almost 2 orders of magnitude less than PSR B1509–58. Also, PSR J0007+7303 shows no strong pulsed radio and X-ray emission like PSR B1509–58 (Halpern et al. 2004), is about 10 times older, and has a higher  $\gamma$ -ray efficiency than PSR B1509–58. Finally, the pulse profiles and spectral behavior of PSR J0007+5303 can be explained nicely with an outer-magnetosphere model unlike PSR B1509–58.

## 5.2. Constraints on the Emission Models in the Nebula

High-energy photons coming from pulsar magnetospheres are usually expected to have a power-law spectrum with an

**Table 4**  
Parameters Derived from the Multi-wavelength Spectral Modeling

Parameter	Value
$p_1$ .....	1.5
$p_2$ .....	2.9
$E_{br}$ (eV).....	$4.6 \times 10^{11}$
$E_{max}$ (eV).....	$2.6 \times 10^{14}$
$B$ ( $\mu\text{G}$ ).....	17
$W_e$ (erg).....	$3.0 \times 10^{48}$
$W_p$ (erg).....	$1.2 \times 10^{51}(1.0/n)$
$L_{sy}$ ( $\text{erg s}^{-1}$ )...	$3.9 \times 10^{36}$
$L_{ic}$ ( $\text{erg s}^{-1}$ )...	$3.1 \times 10^{35}$

exponential cutoff at a few GeV (Abdo et al. 2010a). Kuiper et al. (1999) suggested that PSR B1509–58 has a spectral cutoff or break below 100 MeV. Therefore, the absence of a pulsed signal above 1 GeV, the spatial coincidence, and the similar extension of the LAT source with the PWN as seen in X-rays and very high energy  $\gamma$ -rays strongly suggest that the unpulsed  $\gamma$ -ray emission detected by the LAT above 1 GeV is dominated by the PWN.

There are two possible interpretations for the origins of  $\gamma$ -ray photons from PWNe, i.e., hadronic (from proton–proton interactions) or leptonic (via the inverse Compton process). The multi-wavelength picture of MSH 15–52 is presented in Figure 6 using all available data on MSH 15–52 as reported in Nakamori et al. (2008). The *Fermi*-LAT spectral points, obtained from the analysis described in Section 4.2.2, provide new constraints on the model parameters. A simple one-zone model described in Nakamori et al. (2008) can be used to reproduce the multi-wavelength spectrum of the PWN. We use the publicly distributed<sup>65</sup> ISRF as described in Porter & Strong (2005) as target photons for inverse Compton scattering. The ISRF spectra are modeled and given as a function of cylindrical coordinates in the Galaxy, for IR photons from interstellar dust grains, optical light from normal stars, and CMB. We do not consider the production of  $\gamma$ -rays via bremsstrahlung because of the low density of this region (up to  $\sim 0.4 \text{ cm}^{-3}$ ) as reported in Dubner et al. (2002). For simplicity, escape, energy, and adiabatic losses as well as the time evolution of the magnetic field strength in the PWN are neglected, since the characteristic age of the pulsar is quite young. As reported by Nakamori et al. (2008), a single power-law electron spectrum does not reproduce the SED; hence the accumulated electron spectrum used here follows a broken power law with an exponential cutoff

$$\frac{dN_e}{dE} \propto \frac{(E/E_{br})^{-p_1}}{1 + (E/E_{br})^{p_2-p_1}} \exp\left(-\frac{E}{E_{max}}\right), \quad (3)$$

where  $E_{max}$ ,  $E_{br}$ ,  $p_1$ , and  $p_2$  are the maximal energy, break energy, and the indices of the electron spectrum, respectively. The best fit yields the parameters listed in Table 4 and is overlaid in Figure 6.

The fitted mean magnetic field strength of 17  $\mu\text{G}$  is identical with the value suggested by TeV observations (Aharonian et al. 2005; Nakamori et al. 2008) and consistent with the lower limit of  $\geq 8 \mu\text{G}$  obtained from X-ray data (Gaensler et al. 2002). We confirm that the  $\gamma$ -ray emission from the PWN is dominated by the inverse Compton scattering of the IR photons from interstellar dust grains with a radiation density fixed at

<sup>65</sup> GALPROP model of cosmic-ray transport:  
[http://galprop.stanford.edu/web\\_galprop/galprop\\_home.html](http://galprop.stanford.edu/web_galprop/galprop_home.html)

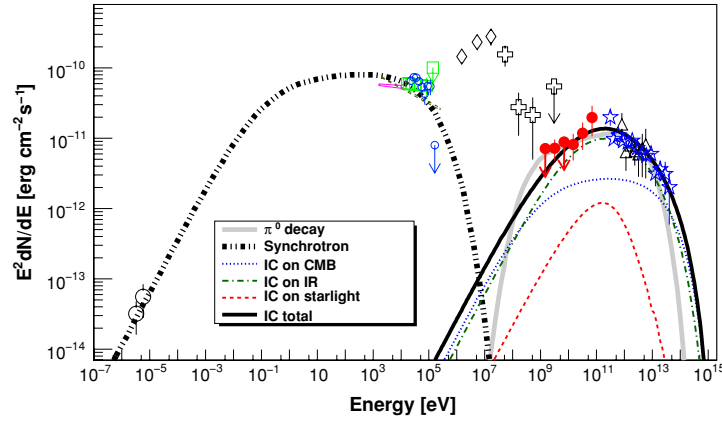


**Figure 6.** SED of the PWN powered by PSR B1509–58, from radio to very high energy  $\gamma$ -rays. Predicted spectra as discussed in Section 5.2 are overlaid. The total IC spectrum is shown with a solid line while thinner lines denote the individual IC components: CMB (dotted), infrared (dot-dashed), and optical (dashed). The triple-dot-dashed line indicates the corresponding synchrotron emission. A hadronic  $\gamma$ -ray model is also overlaid by a thick gray curve. Observational data points: ATCA (open circles; Gaensler et al. 1999; Gaensler et al. 2002), *BeppoSAX*/MECS (magenta thin line region; Mineo et al. 2001), *BeppoSAX*/PDS (light green open squares; Forot et al. 2006 and the upper limit is  $1\sigma$ ), *INTEGRAL*/IBIS (dark blue open circles; Forot et al. 2006 and the upper limit is  $1\sigma$ ), *RXTE*/PCA+HEXTE (dark green dashed line region; Marsden et al. 1997), COMPTEL (open diamonds; Kuiper et al. 1999), EGRET (open crosses; Kuiper et al. 1999), *Fermi*-LAT (this paper, filled circles), H.E.S.S. (open stars; Aharonian et al. 2005), and CANGAROO-III (open triangles; Nakamori et al. 2008). Note that COMPTEL and EGRET points present the DC emission from this region, which is dominated by the central pulsar for this energy range and could be contaminated by the nearby  $\gamma$ -ray pulsar PSR J1509–5850 recently identified by the LAT (Abdo et al. 2010a).

(A color version of this figure is available in the online journal.)

$1.4 \text{ eV cm}^{-3}$ , which is the nominal value of the GALPROP ISRF. Here, the contribution of the optical photon field is negligible because of the Klein–Nishina effect (Klein & Nishina 1929).

The nature of the break energy  $E_{\text{br}}$  remains unclear. A radiation cooling break which is dominated by the synchrotron loss in this leptonic scenario is a primary candidate. With the assumed magnetic field ( $B = 17 \mu\text{G}$ ) and system age ( $\tau = 1.7 \text{ kyr}$ ), the break energy can be calculated using standard formulae in Pacholczyk (1970) as  $6\pi m_e^2 c^3 / B^2 \sigma_T \tau \sim 24 \text{ TeV}$  leading to a break in the photon spectrum at  $36(B/1 \mu\text{G})(\tau/10^3 \text{ yr})^{-2} \text{ eV} \sim 0.2 \text{ keV}$ . Even considering the limit of the one-zone approximation and potential uncertainty in the parameters obtained, the fitted value of 460 GeV, which predicts a break in the photon spectrum at  $\sim 8 \times 10^{-3} \text{ eV}$ , is much lower than the expected value. However, the photon index change  $\Delta\Gamma = 0.7$  is compatible with the prediction by the usual synchrotron cooling  $\Delta\Gamma = 0.5$ . One should note that the synchrotron break in this PWN is expected to occur just below the X-ray band and no hints of a break have yet been observed. More likely, this break energy could be an intrinsic characteristic of the electron spectrum injected in the PWN as suggested by de Jager (2008), though  $p_2 = 2$  is expected. Another possibility would be that the spectral break of electrons may correspond to the energy scale where the electron acceleration mechanism switches, for instance, from magnetic reconnection (Zenitani & Hoshino 2001) to the usual first-order Fermi acceleration. However, while Zenitani & Hoshino (2001) indeed predict an index of unity, the production of an index harder than 2 is explained with difficulty by Fermi acceleration.

The total energy PSR B1509–58 can supply to its PWN is strongly dependent on its initial spin period  $P_0$ , which is generally unknown, as  $E_{\text{tot}} = 2\pi^2 I (\frac{1}{P_0^2} - \frac{1}{P^2})$ , where  $I$  is the moment of inertia of the neutron star.  $P_0$  can be analytically calculated for an ideal case, assuming that  $k$  and  $n$  are constant in the braking equation  $\dot{\Omega} = -k\Omega^n$  (Gaensler & Slane 2006). Using the standard parameters of the pulsar PSR B1509–58 (period of 150 ms, period derivative of  $1.5 \times 10^{-12} \text{ s s}^{-1}$ , and braking index  $n = 2.84$ ; Livingstone et al. 2005), we obtain  $P_0 = 16 \text{ ms}$  and  $E_{\text{tot}} = 7.5 \times 10^{49} \text{ erg}$ . Knowing that the fit requires a total injected energy (i.e., integrated electron

energies above 1 GeV) of  $W_e = 3.0 \times 10^{48} \text{ erg}$ ,  $\sim 4\%$  of  $E_{\text{tot}}$  should be converted into the current kinetic energy of electrons.

The equipartition magnetic field strength can be estimated as  $B_{\text{eq}} = \sqrt{8\pi W_e / V}$ , where  $V$  is a volume of the emission region. Assuming a spherical region of radius  $r$ , we obtain  $B_{\text{eq}} = 22(10 \text{ pc}/r)^{3/2} \mu\text{G}$ . In the case of the considered source where  $r \sim 10 \text{ pc}$ , the PWN is particle dominated as suggested by Chevalier (2004). The measurement of the extension of the HE  $\gamma$ -ray emission is of particular interest to better estimate the boundary of the PWN.

We also consider a  $\pi^0$  decay model, assuming a proton spectrum described by a power law with a cutoff to fit the data points, though there are few theoretical indications supporting an injection of such hard protons. We obtain an index of protons of 1.9 with a cutoff energy of 60 TeV, which yields the accumulated energy of protons above 1 GeV of  $1.2 \times 10^{51} (1.0 \text{ cm}^3)/n \text{ erg}$ , where  $n$  is the number density of target nuclei. This scenario is highly disfavored from the energetics: even with a very high density of  $\sim 10 \text{ cm}^{-3}$  as mentioned by Dubner et al. (2002) for the northwest limb of MSH 15–52, the energy required would significantly exceed the total energy that the pulsar can supply to its nebula ( $E_{\text{tot}} = 7.5 \times 10^{49} \text{ erg}$ ).

## 6. CONCLUSION

We report the detection of pulsed high-energy  $\gamma$ -rays from PSR B1509–58 below 1 GeV and extended emission from its PWN in MSH 15–52 up to 100 GeV using 1 yr of survey data with *Fermi*-LAT. The LAT light curve of PSR B1509–58 above 30 MeV presents two peaks. The  $\gamma$ -ray pulse located at phase  $0.33 \pm 0.02$  is coincident with the main peak observed in X- and soft  $\gamma$ -rays (Ulmer et al. 1993; Kuiper et al. 1999). The second peak detected at phase  $0.96 \pm 0.01$  may correspond to the marginal detection reported by Kuiper et al. (1999) in the 10–30 MeV energy range covered by EGRET. The high-altitude emission models have problems explaining the peak separation measured with *Fermi* and the radio peak lagging the first  $\gamma$ -peak. A confirmation of a possible precursor in the 1351 MHz radio profile (Crawford et al. 2001) might change this interpretation.

The  $2\sigma$  upper limits derived below 1 GeV confirm the spectral break of PSR B1509–58 in the 10–30 MeV energy range. More data are needed to measure the pulsar spectrum in the LAT energy range. Such estimates can help constrain the shape of the spectrum from X- to  $\gamma$ -rays and disentangle between the emission models in the magnetosphere of PSR B1509–58. Both the high-altitude models (Romani 1996; Venter et al. 2009) and the PC model (Harding et al. 1997) can accommodate the severe spectral break and the low *Fermi* limits. Details such as the break energy and/or X-ray spectral shape are not exactly met. The extended  $\gamma$ -ray emission observed by the LAT above 1 GeV is spatially coincident with the PWN powered by PSR B1509–58. Its morphology is well modeled by a uniform disk or a Gaussian distribution. The LAT spectrum of the PWN above 1 GeV is well described by a power law with a photon index of  $(1.57 \pm 0.17 \pm 0.13)$  and a flux above 1 GeV of  $(2.91 \pm 0.79 \pm 1.35) \times 10^{-9} \text{ cm}^{-2} \text{ s}^{-1}$ . LAT analyses of the PWN in MSH 15–52 bring new elements to the discussion on the emission models responsible for the high to very high emission from this source. The hadronic  $\gamma$ -ray scenario is highly disfavored by the new LAT observations, as suggested by previous TeV observations (Aharonian et al. 2005; Nakamori et al. 2008). The multi-wavelength spectrum can be explained by synchrotron and inverse Compton processes, assuming a broken power-law spectrum for the electrons. The spectral break, constrained by multi-wavelength observations, is likely due to an intrinsic break of electrons injected from the pulsar wind. About 4% of the pulsar's loss of rotational energy would be required to power the  $\gamma$ -rays detected by the LAT, well in the range observed for other PWNe. More data are required to estimate the detailed morphology of the high-energy  $\gamma$ -ray emission and better constrain the spectral break in the inverse Compton component.

The *Fermi*-LAT Collaboration acknowledges generous ongoing support from a number of agencies and institutes that have supported both the development and the operation of the LAT as well as scientific data analysis. These include the National Aeronautics and Space Administration and the Department of Energy in the United States, the Commissariat à l'Énergie Atomique and the Centre National de la Recherche Scientifique/Institut National de Physique Nucléaire et de Physique des Particules in France, the Agenzia Spaziale Italiana and the Istituto Nazionale di Fisica Nucleare in Italy, the Ministry of Education, Culture, Sports, Science and Technology (MEXT), High Energy Accelerator Research Organization (KEK) and Japan Aerospace Exploration Agency (JAXA) in Japan, and the K. A. Wallenberg Foundation, the Swedish Research Council and the Swedish National Space Board in Sweden.

Additional support for science analysis during the operations phase is gratefully acknowledged from the Istituto Nazionale di Astrofisica in Italy and the Centre National d'Études Spatiales in France.

The Parkes radio telescope is part of the Australia Telescope which is funded by the Commonwealth Government for operation as a National Facility managed by CSIRO. We thank our colleagues for their assistance with the radio timing observations.

## REFERENCES

- Abdo, A. A., et al. 2008, *Science*, **322**, 1218  
 Abdo, A. A., et al. 2010a, *ApJS*, **187**, 460  
 Abdo, A. A., et al. 2010b, *ApJS*, submitted (arXiv:1002.2280)  
 Abdo, A. A., et al. 2010c, *ApJ*, **710**, L92  
 Abdo, A. A., et al. 2010d, *ApJ*, **713**, 146  
 Abdo, A. A., et al. 2010e, *ApJ*, **708**, 1254  
 Aharonian, F. A., et al. 2005, *A&A*, **435**, L17  
 Atwood, B. W., et al. 2009, *ApJ*, **697**, 1071  
 Baring, M. G. 2004, *Adv. Space Res.*, **33**, 552  
 Bednarek, W., & Bartosik, M. 2003, *A&A*, **405**, 689  
 Caswell, J. L., Milne, D. K., & Wellington, K. J. 1981, *MNRAS*, **195**, 89  
 Cheng, K. S., Ruderman, M., & Zhang, L. 2000, *ApJ*, **537**, 964  
 Cheng, K. S., et al. 1986, *ApJ*, **300**, 500  
 Chevalier, R. A. 2004, *Adv. Space Res.*, **33**, 456  
 Cordes, J. M., & Lazio, T. J. W. 2002, arXiv:astro-ph/0207156  
 Crawford, F., et al. 2001, *Astron. J.*, **122**, 2001  
 Cusumano, G., et al. 2001, *A&A*, **375**, 397  
 Daugherty, J. K., & Harding, A. K. 1996, *ApJ*, **458**, 278  
 de Jager, O. C. 2008, *ApJ*, **678**, L113  
 de Jager, O. C., Raubenheimer, B. C., & Swanepoel, J. W. H. 1989, *A&A*, **221**, 180  
 Dubner, G. M., et al. 2002, *AJ*, **123**, 337  
 Dyks, J., & Rudak, B. 2003, *ApJ*, **598**, 1201  
 Forot, M., Hermsen, W., Renaud, M., Laurent, P., Greiner, I., Goret, P., Khelifi, B., & Kuiper, L. 2006, *ApJ*, **651**, L45  
 Gaensler, B. M., Brazier, K. T. S., Manchester, R. N., Johnston, S., & Green, A. J. 1999, *MNRAS*, **305**, 724  
 Gaensler, B. M., & Slane, P. O. 2006, *ARA&A*, **44**, 17  
 Gaensler, B. M., et al. 2002, *ApJ*, **569**, 878  
 Halpern, J. P., et al. 2004, *ApJ*, **612**, 398  
 Harding, A., Baring, M., & Gonthier, P. 1997, *ApJ*, **476**, 246  
 Hobbs, G. B., et al. 2004, *MNRAS*, **352**, 1439  
 Hobbs, G. B., et al. 2006, *MNRAS*, **369**, 655  
 Horns, D. 2006, *A&A*, **451**, L51  
 Kaspi, V. M., Manchester, R. N., Siegelman, B., Johnston, S., & Lyne, A. G. 1994, *ApJ*, **422**, L83  
 Kawai, N., et al. 1991, *ApJ*, **383**, L65  
 Kennel, C. F., & Coroniti, F. V. 1984, *ApJ*, **283**, 694  
 Klein, O., & Nishina, Y. 1929, *Z. Phys.*, **52**, 853  
 Kuiper, L., et al. 1999, *A&A*, **351**, 119  
 Livingstone, M. A., Kaspi, V. M., Gavriil, F. P., & Manchester, R. N. 2005, *ApJ*, **619**, 1046  
 Lyne, A. G., & Manchester, R. N. 1988, *MNRAS*, **234**, 477  
 Manchester, R. N. 2008, in *AIP Conf. Proc.* 983, 40 Years of Pulsars: Millisecond Pulsars, Magnetars and More, ed. C. Bassa et al. (Melville, NY: AIP), **584**  
 Manchester, R. N., & Taylor, J. H. 1977, *Pulsars* (San Francisco, CA: Freeman), **36**  
 Manchester, R. N., Tuohy, I. R., & Damico, N. 1982, *ApJ*, **262**, L31  
 Marsden, D., et al. 1997, *ApJ*, **491**, L39  
 Mattox, J. R., et al. 1996, *ApJ*, **461**, 396  
 Mineo, T., Cusumano, G., Maccarone, M. C., Massaglia, S., Massaro, E., & Trussoni, E. 2001, *A&A*, **380**, 695  
 Muslimov, A. G., & Harding, A. K. 2004, *ApJ*, **606**, 1143  
 Nakamori, T., et al. 2008, *ApJ*, **677**, 297  
 Pacholczyk, A. G. 1970, *Radio Astrophysics* (San Francisco, CA: Freeman)  
 Pellizzoni, A., et al. 2009, *ApJ*, **695**, L115  
 Porter, T. A., & Strong, A. W. 2005, *Proc. 29th ICRC (Pune)*, **4**, 77  
 Radhakrishnan, V., & Cooke, D. J. 1969, *Astrophys. Lett.*, **3**, L225  
 Romani, P. W. 1996, *ApJ*, **470**, 469  
 Rots, A. H., et al. 1998, *ApJ*, **501**, 749  
 Sako, T., et al. 2000, *ApJ*, **537**, 422  
 Seward, F. D., & Harden, F. R. 1982, *ApJ*, **256**, L45  
 Smith, D. A., et al. 2008, *A&A*, **492**, 923  
 Strong, A. W., Moskalenko, I. V., & Reimer, O. 2004a, *ApJ*, **613**, 962  
 Strong, A. W., Moskalenko, I. V., Reimer, O., Digel, S., & Diehl, R. 2004b, *A&A*, **422**, L47  
 Tamura, K., Kawai, N., Yoshida, A., & Brinkmann, W. 1996, *PASJ*, **48**, L33  
 Trussoni, E., et al. 1996, *A&A*, **306**, 581  
 Ulmer, M. P., et al. 1993, *ApJ*, **417**, 738  
 Venter, C., Harding, A. K., & Guillemot, L. 2009, *ApJ*, **707**, 800  
 Watters, K. P., Romani, R. W., Weltevrede, P., & Johnston, S. 2009, *ApJ*, **695**, 1289  
 Weltevrede, P., et al. 2010, *PASA*, **27**, 64  
 Yatsu, Y., Kawai, N., Shibata, S., & Brinkmann, W. 2009, *PASJ*, **61**, 129  
 Zenitani, S., & Hoshino, M. 2001, *ApJ*, **562**, L63  
 Zhang, L., & Cheng, K. S. 2001, *A&A*, **363**, 575